Spin-tensor Meissner currents of ultracold bosonic gases in an optical lattice

Xiaofan Zhou [1,2] Suotang Jia,[1,2] and Xi-Wang Luo[3,4,*]

[1]*State Key Laboratory of Quantum Optics and Quantum Optics Devices, Institute of Laser Spectroscopy, Shanxi University, Taiyuan 030006, China*

[2]*Collaborative Innovation Center of Extreme Optics, Shanxi University, Taiyuan, Shanxi 030006, China*

[3]*CAS Key Laboratory of Quantum Information, University of Science and Technology of China, Hefei, Anhui 230026, China*

[4]*Synergetic Innovation Center of Quantum Information and Quantum Physics, University of Science and Technology of China, Hefei, Anhui 230026, China*

We investigate the Meissner currents of interacting bosons subjected to a staggered artificial gauge field in a three-leg ribbon geometry, realized by spin-tensor–momentum coupled spin-1 atoms in a one-dimensional optical lattice. By calculating the current distributions using the state-of-the-art density-matrix renormalization-group method, we find a rich phase diagram containing interesting Meissner and vortex phases, where the currents are mirror symmetric with respect to the middle leg (i.e., they flow in the same direction on the two boundary legs, opposite to that on the middle leg), leading to spin-tensor-type Meissner currents, which is very different from previously observed chiral edge currents under uniform gauge field. The currents are uniform along each leg in the Meissner phase and form vortex-antivortex pairs in the vortex phase. Moreover, the system also supports a polarized phase that spontaneously breaks the mirror symmetry, whose ground states are degenerate with currents either being uniform or forming vortex-antivortex pairs. We also discuss the experimental schemes for probing these phases. Our work provides useful guidance for ongoing experimental research on synthetic flux ribbons and paves the way for exploring novel many-body phenomena therein.

I. INTRODUCTION

Charged particles in a magnetic field showcase a remarkable variety of macroscopic quantum phenomena, including quantized Hall resistance in topological insulators [1,2] and the Meissner effect in superconductors [3,4]. Recent experimental advances in realizing synthetic gauge fields in ultracold atomic systems provide a powerful tool for exploring these novel phenomena in a fully controllable, clean environment [5–12]. Chiral Meissner (topological edge) currents have been observed experimentally with an atomic Bose (Fermi) gas in both ladder [13,14] and three-leg ribbon geometries [15,16], where the two-dimensional (2D) lattice consists of the sites of a one-dimensional (1D) optical lattice in the long direction and internal atomic spin states forming a synthetic lattice in the short direction. Such synthetic dimensions enable the investigation of higher-dimensional physics beyond the physical dimensions of the systems and bring new opportunities to explore novel quantum phenomena [17–19]. The experimentally observed chiral currents result from a uniform gauge field that is equivalent to ordinary spin-orbit coupling (i.e., spin-vector–momentum coupling) with the form qF_z, where q is the quasimomentum along the optical lattice direction and $\mathbf{F} = \{F_x, F_y, F_z\}$ are the spin vectors [20]. Consequently, the corresponding Meissner currents also exhibit

spin-vector properties; that is, atoms with opposite spins propagate along opposite directions [14–16,21].

For higher-spin ($\geqslant 1$) systems (e.g., the synthetic three-leg ribbon), it is well known that not only spin vectors but also spin tensors exist [22,23]. Spin-tensor–momentum coupling (STMC) in the form qF_z^2 was proposed and experimentally realized recently [24,25], which could significantly modify the band structures (e.g., dark-state band, triply degenerate points) and lead to interesting many-body physics (e.g., magnetic stripe phase) in the presence of interactions [25–29]. It was also shown that STMC in a 1D Mott bosonic lattice can support interesting spin-tensor magnetism orders [30]. So far, studies on Meissner effects have focused on the aforementioned spin-vector types with uniform synthetic gauge fields. Therefore, a natural and important step is to explore the Meissner effects of interacting atoms in optical lattices with STMC.

In this paper, we investigate the ground-state Meissner currents of spin-tensor–momentum coupled spin-1 bosons in a 1D optical lattice using state-of-the-art density-matrix renormalization-group (DMRG) numerical methods [31,32]. The system corresponds to a synthetic three-leg ribbon with a staggered gauge field, where the magnetic domain wall is given by the middle leg. We are interested in the Meissner effects and distinguish different phases by examining the current and momentum distributions. In the noninteraction limit, there are two phases depending on the minima of the lowest single-particle band. The Meissner (M) phase with a single band minimum occurs when the interleg couplings are strong,

*luoxw@ustc.edu.cn

where the Meissner current is uniform along each leg, with its amplitude determined by the gauge field strength. As the interleg coupling decreases across some critical value, the system undergoes a transition to the vortex (V) phase with double band minima, where atoms can occupy both minima and their interference can lead to vortex structures of the currents, forming vortex-antivortex pairs. For both the M and V phases, the current distributions are always mirror symmetric with respect to the middle leg; they have a rank-2 spin-tensor form which is very different from the spin-vector Meissner current. In particular, here, the current flows in the same direction on the two boundary legs, opposite to the current direction on the middle leg. Meanwhile, the rank-0 scalar charge current and rank-1 spin-vector current are both zero.

In the presence of interaction, the phase diagram is altered significantly. In the weak-interaction region, ferromagnetic spin-spin interaction can dominate over density-density interaction and stabilize the V phase with equal populations on the two band minima. In the strong-interaction region, the wave packet becomes broadened in the momentum space, and the two wave packets at the two band minima merge into one, and thus, the system favors the M phase even when the lowest band has two minima. Interestingly, for intermediate-interaction strength, the spin-spin interaction can induce a new polarized (P) phase that spontaneously breaks the mirror symmetry with respect to the middle leg, although the STMC (i.e., synthetic gauge field) preserves such symmetry. In the P phase, atoms start to occupy the dark middle band induced by the STMC, and the ground states are degenerate, with currents either being uniform or forming vortex-antivortex pairs. The P phase resulting from the presence of the dark middle band is unique for STMC systems and is absent for spin-vector-coupled systems. The Meissner currents in all phases persist regardless of whether the system belongs to a superfluid or Mott insulator.

II. MODEL AND HAMILTONIAN

We consider an experimental setup based on a Bose-Einstein condensate in a 1D optical lattice with STMC, as shown in Fig. 1(a). A pair of counterpropagating lasers with wavelength λ_L (green arrows) is used to realize the 1D optical lattices $V_{lat}(y) = -V_0 \cos^2(k_L y)$ along the y direction, with wave number $k_L = 2\pi/\lambda_L$. Three Raman lasers, R_1 (yellow), R_2 (blue), and R_3 (red), with wavelength λ_Ω and an incident angle η with respect to lattice direction, induce two Raman transitions between spin states $|0\rangle$ and $|\uparrow(\downarrow)\rangle$ accompanied by the momentum transfer $2k_R$ [24], where $k_R = 2\pi \cos(\eta)/\lambda_\Omega$, as shown in Fig. 1(b). The tight-binding Hamiltonian reads

$$H = -t \sum_{\langle j,j' \rangle, \sigma} \hat{b}_{j\sigma}^\dagger \hat{b}_{j'\sigma} + \frac{\Omega}{\sqrt{2}} \sum_j (e^{i\phi j} \hat{b}_{j0}^\dagger \hat{b}_{j+} + \text{H.c.})$$
$$+ \sum_j \frac{U_0}{2} \hat{n}_j(\hat{n}_j - 1) + \frac{U_2}{2}(\mathbf{S}_j^2 - 2\hat{n}_j) + \delta S_{j,z}^2, \quad (1)$$

where $\hat{b}_{j\sigma}^\dagger$ ($\hat{b}_{j\sigma}$) is the Bose creation (annihilation) operator with spin basis $\sigma = \{\uparrow, 0, \downarrow\}$ and $\hat{b}_{j\pm} = (\hat{b}_{j\uparrow} \pm \hat{b}_{j\downarrow})/\sqrt{2}$. The particle number operator is $\hat{n}_j = \sum_\sigma \hat{n}_{j\sigma}$, with $\hat{n}_{j\sigma} = \hat{b}_{j\sigma}^\dagger \hat{b}_{j\sigma}$. t is the tunneling amplitude between neighboring
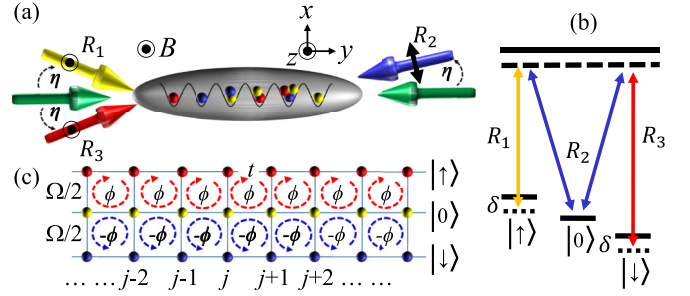

FIG. 1. (a) Schematics of the system setup. The ultracold atoms are trapped in a 1D optical lattice, which is generated by a pair of counterpropagating lasers with wavelength λ_L (green arrows). Three Raman lasers (yellow, blue, and red arrows) with wavelength λ_Ω and angle η with respect to the y direction induce two Raman transitions. (b) Raman transitions between spin states $|0\rangle$ and $|\uparrow(\downarrow)\rangle$ with detuning δ. (c) The effective three-leg ribbon with a staggered gauge field along the synthetic dimension.

lattice sites, and Ω is the Raman coupling strength. The flux $\phi = 2\pi \cos(\eta)\lambda_L/\lambda_\Omega = 2\cos(\eta)k_R a$ can be tuned by tuning the angle η. δ is the detuning for both the $|\uparrow\rangle$ and $|\downarrow\rangle$ states. For simplicity, we set $\delta = 0$ in the following. U_0 and U_2 are the density-density and spin-spin on-site interactions, which are related to the scattering lengths $a_{0,2}$ (corresponding to the channels with total spin 0 and 2, respectively) as $U_0 = 4\pi\hbar^2(a_0 + 2a_2)/3M$ and $U_2 = 4\pi\hbar^2(a_2 - a_0)/3M$, where M is the mass of the atom [33,34]. The spin-dependent interaction is antiferromagnetic for ^{23}Na for $U_2/U_0 > 0$ and ferromagnetic for ^{87}Rb for $U_2/U_0 < 0$. $\mathbf{S}_j = \sum_{\sigma\acute{\sigma}} \hat{b}_{j\sigma}^\dagger \mathbf{F}_{\sigma\acute{\sigma}} \hat{b}_{j\acute{\sigma}}$ is the total spin at site j, where $\mathbf{F}_{\sigma\acute{\sigma}}$ represent the matrix elements of the spin-vector operator. We also set t as the energy unit.

III. PHASE DIAGRAM

A. Band structures

We first discuss the single-particle band structure of the system. Effectively, the system corresponds to a three-leg ribbon with a staggered gauge field, as shown in Fig. 1(c). After a unitary transformation the Hamiltonian without interaction can be written as

$$H_0 = -t e^{i\phi\gamma_\sigma} \sum_{\langle j,j' \rangle, \sigma} \hat{c}_{j\sigma}^\dagger \hat{c}_{j'\sigma} + \frac{\Omega}{\sqrt{2}} \sum_j (\hat{c}_{j0}^\dagger \hat{c}_{j+} + \text{H.c.}), \quad (2)$$

where $(\hat{c}_{j\uparrow}, \hat{c}_{j0}, \hat{c}_{j\downarrow})^T = U(\hat{b}_{j\uparrow}, \hat{b}_{j0}, \hat{b}_{j\downarrow})^T$, with $U = \exp(i\phi j F_z^2)$, and $\gamma_\uparrow = 1$, $\gamma_0 = 0$, and $\gamma_\downarrow = 1$. Then, we Fourier transform the Hamiltonian and obtain

$$H_0 = \sum_q \hat{C}_q^\dagger \left[-2t \cos\left(qa + \phi F_z^2\right) + \frac{\Omega}{\sqrt{2}} F_x \right] \hat{C}_q, \quad (3)$$

where $\hat{C}_q = (\hat{c}_{q\uparrow}, \hat{c}_{q0}, \hat{c}_{q\downarrow})^T$ is the corresponding operator in quasimomentum q space, $a = \pi/k_L$ is the lattice constant, and F_z^2 is the rank-2 spin tensor. We see that the flux ϕ now represents the strength of the STMC. The system exhibits three bands after we diagonalize the Hamiltonian (3), as shown in Fig. 2(a). The top and bottom bright-state bands exhibit the same behavior as a spin-orbit-coupled spin-1/2 system with
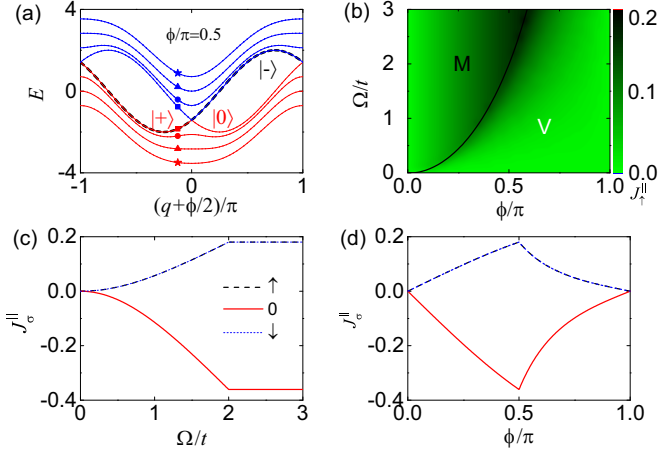
FIG. 2. (a) Single-particle band structure of the Hamiltonian (3) for different values of Ω/t with flux $\phi/\pi = 0.5$ and $\Omega_c/t = 2$. The system exhibits three bands, including the upper band (blue line), the lowest band (red line), and the middle band (black dashed line). Blue (red) lines with different markers correspond to the upper (lowest) band with different Ω; the squares, dots, triangles, and stars mark the bands with $\Omega/t = 0, 1, 2, 3$, respectively. The middle band is the dark band with spin state $|-\rangle$ and is unaffected by Ω. The spin components $|0\rangle$ and $|+\rangle$ are indicated around the corresponding band minima. The lowest band has a single minimum for $\Omega > \Omega_c$ and two symmetric band minima for $\Omega < \Omega_c$. (b) The noninteracting phase diagram in the Ω-ϕ plane, with vortex (V) and Meissner (M) quantum phases. The color bar denotes the current $J_\uparrow^\parallel$, and the solid line is the critical line given by Ω_c. The profiles of the current J_σ^0 as a function of Ω and ϕ, respectively, with (c) $\phi/\pi = 1/2$ and (d) $\Omega/t = 2.0$. The filling factor is $\rho = 1.0$ in (b)–(d). We set t as the energy unit.

spin states $|0\rangle$ and $|+\rangle = (|\uparrow\rangle + |\downarrow\rangle)/\sqrt{2}$ [see the colored lines in Fig. 2(a)]. The middle band $E_q = -2t\cos(q + \phi)$ is a dark-state band which always has the spin state $|-\rangle = (|\uparrow\rangle - |\downarrow\rangle)/\sqrt{2}$ and is independent of Ω [see the black dashed line in Fig. 2(a)] since it is decoupled from the Raman lasers. However, the dark-state band plays an important role in both ground-state and Meissner current distributions in the presence of interactions.

B. Order parameters

Before we calculate the phase diagram of the system, in the following, we first introduce some order parameters that we will use to distinguish different phases.

Currents. Since we are interested in the Meissner effects, the most important property here is the current along the legs and the rungs of the ribbon. Local averaged currents along the leg direction can be defined as [13,14,35,36]

$$J_{j,\sigma}^\parallel = it\langle \hat{b}_{j+1\sigma}^\dagger \hat{b}_{j\sigma} - \text{H.c.}\rangle, \quad J_\sigma^\parallel = \frac{1}{L}\sum_j J_{j,\sigma}^\parallel. \quad (4)$$

Similarly, we can define the rung currents along the synthetic direction [14,36],

$$J_{j,0s}^\perp = i\Omega\langle e^{i\phi j}\hat{b}_{j0}^\dagger \hat{b}_{js} - \text{H.c.}\rangle, \quad (5)$$

with $s = \{\uparrow, \downarrow\}$. We then introduce the current orders

$$I_{0s}^\perp = \frac{1}{L}\sum_j |J_{j,0s}^\perp|, \quad I_z^\parallel = \frac{1}{L}\sum_j |J_{j,\uparrow}^\parallel - J_{j,\downarrow}^\parallel|. \quad (6)$$

The rungs current order $I_{0s}^\perp$ distinguishes the M phase (with vanishing $I_{0s}^\perp$) from the V phase (with finite $I_{0s}^\perp$). The leg current order $I_z^\parallel$ characterizes the current polarization associated with the mirror symmetry with respect to the middle leg (a nonvanishing $I_z^\parallel$ represents the breaking of the mirror symmetry). Different phases can be identified by different current distributions and orders.

Spin moments. Experimentally, the spin moments of the atoms can be measured by spin-selective imaging of the density distributions

$$n_{j,\sigma} = \langle \hat{b}_{j\sigma}^\dagger \hat{b}_{j\sigma}\rangle. \quad (7)$$

The density distributions can be measured either in the basis $\sigma = \{\uparrow, 0, \downarrow\}$ or in the basis $\sigma = \{0, \pm\}$. We can define the spin-moment orders as

$$n_\sigma = \frac{1}{L}\sum_j n_{j,\sigma}, \quad (8)$$

which gives the population properties of the bands and can be used to characterize the phase transition. We note that n_- corresponds to the occupation of the dark middle band.

Entropy. The many-body interacting phase diagram can be further confirmed by the entanglement entropy. Sharp features emerge at the critical points in the von Neumann entropy, defined as [37–43]

$$S_{\text{vN}} = -\text{Tr}_A[\hat{\rho}_A \ln \hat{\rho}_A], \quad (9)$$

where $\hat{\rho}_A = \text{Tr}_B|\psi\rangle\langle\psi|$ is the reduced density matrix and $|\psi\rangle$ is the ground-state wave function, with A and B corresponding to the left and right halves of the 1D chain.

Low-energy-level spacing. The energy-level spacing with respect to the ground-state energy, defined as

$$\Delta_i = E_i - E_0, \quad (10)$$

may also be used to signal the phase transition. Here, E_0 is the lowest eigenenergy, and E_i is the ith-order eigenenergy with fixed particle numbers.

C. Noninteracting phase diagram

In the noninteracting limit, the phase diagram is determined by the single-particle band structures. The lowest band presents a single minimum in the M phase, $\Omega > \Omega_c$, and two symmetric minima in the V phase, $\Omega < \Omega_c$, where Ω_c is the critical coupling strength, as shown in Fig. 2(a). According to the number of minima, we can plot the single-particle phase diagram in the Ω-ϕ plane, as shown in Fig. 2(b), which is similar to the phase diagram of a spin-1/2 spin-orbit-coupled system [14]. However, the currents have a rank-2 spin-tensor form that is very different from the spin-vector Meissner current [14,16]. In particular, here, the current flows in the same direction on the boundary legs, opposite to the current direction on the middle leg. We calculate the ground-state currents of Hamiltonian (1); the averaged currents along each leg are shown in Figs. 2(c) and 2(d). It is easy to check
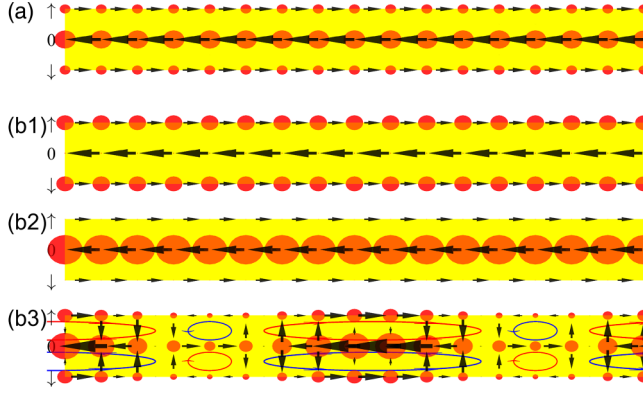
FIG. 3. The schematic of the density distributions $n_{j,\sigma}$ and currents $J_{j,\sigma}^{\parallel}$ and $J_{j,0s}^{\perp}$ in different phases. The points denote the density profile of the three components with point size indicating the number of atoms. The current direction and strength are denoted by the arrows. (a) The M phase with $\Omega/t = 2.5$ and $\phi/\pi = 1/2$. (b1)–(b3) The V phase with $\Omega/t = 0.2$ and $\phi/\pi = 1/4$. (b1) Left minimum ground state [blue dot in Fig. 2(a)]. (b2) Right minimum ground state [red dot in Fig. 2(a)]. (b3) Equal superposition of the two minima.

FIG. 4. (a) The current order parameters $I_z^{\parallel}$ and $I_{0s}^{\perp}$ versus interaction strength U_0. (b) Spin-moment orders $n_{\pm,0}$ versus U_0. (c) Entropy S_{vN} and (d) excited energy gap Δ_i as a function of interaction strength U_0. In all plots, we have $\Omega/t = 0.2$, $\phi/\pi = 1/4$, $U_2 = -0.2U_0$, $\rho = 1.0$, and $L = 64$.

that the rank-0 scalar charge current $J^{\parallel} \equiv \sum_\sigma J_\sigma^{\parallel}$ and rank-1 spin-vector current $J_z^{\parallel} \equiv \sum_\sigma \sigma J_\sigma^{\parallel}$ are both zero, while the rank-2 spin-tensor current $J_{zz}^{\parallel} \equiv \sum_\sigma \sigma^2 J_\sigma^{\parallel} = 2J_\uparrow^{\parallel}$ is finite. As we increase Ω for a fixed ϕ, $J_{zz}^{\parallel}$ increases and has a saturated value above the critical point; as shown in Fig. 2(c), the system undergoes a transition from the V to M phase. For increasing flux ϕ with $\Omega/t = 2.0$, $J_{zz}^{\parallel}$ increases first and then decreases, reaching its maxima at the phase transition point from the M to V phase, as shown in Fig. 2(d).

In order to clearly show the local current properties of the V and M phases, we plot schematics of density distributions $n_{j,\sigma}$ and currents $J_{j,\sigma}^{\parallel}$ and $J_{j,0s}^{\perp}$ in Fig. 3. The current is mirror symmetric with respect to the middle leg, analogous to the combination of the spin-1/2 (two-leg ladder) vector current and its mirror reflection. In the M phase, both the currents and the densities are uniform, as shown in Fig. 3(a). In the V phase, the system exhibits two energy minima in the lowest band. Atoms may populate on either minimum with the same tensor current, as shown in Figs. 3(b1) and 3(b2), or in a linear combination of the two minima with a current vortex, as shown in Fig. 3(b3).

D. Interacting phase diagram

The interplay between the single-particle band structure and the interaction is fundamental to many areas of modern physics. The ability to engineer competing interactions between atoms through lattice depth or Feshbach resonances [44] makes cold atomic systems an ideal platform to generate a rich variety of many-body phenomena [45–51]. Here, we perform state-of-the-art DMRG calculations to calculate the many-body ground states of the system under open boundary conditions. In our numerical simulations, we set the cutoff of the single-site atom number as $n_{\mathrm{cutoff}} = 4$. The effect of such a cutoff can be neglected for strong interactions, while in the weak-interaction region, the phases and phase boundaries may be slightly affected by the cutoff. We find that $n_{\mathrm{cutoff}} = 4$ is
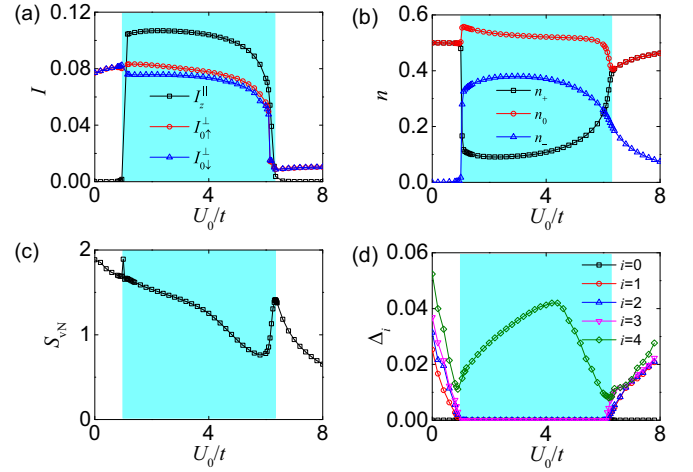
enough to determine the phase boundaries (see Appendix A). We set lattice size up to $L = 64$, for which we retain 300 truncated states per DMRG block and perform 20 sweeps with a maximum truncation error of $\sim 10^{-7}$.

We consider the repulsive density-density interaction with $U_0 > 0$ and ferromagnetic spin-spin interaction with $U_2 < 0$ like for ^{87}Rb and ^{7}Li atoms. In Fig. 4, we plot the order parameters as a function of the interacting strength U_0/t, with fixed $\Omega/t = 0.2$ and $\phi/\pi = 1/4$, from which three phases (i.e., V, P, and M) and their critical boundaries can be identified. For weak interactions, the system stays in the V phase with a large rung current $I_{0s}^{\perp}$; for strong interactions, the system favors the M phase with nearly vanishing $I_{0s}^{\perp}$. We note that finite-size effects would induce a tiny average rung current $I_{0s}^{\perp}$ in the M phase since the leg currents must form a closed loop at the boundary through the rungs. In both the V and M phases, we have $I_z^{\parallel} = 0$ due to the mirror symmetry, although $J_\sigma^{\parallel} \neq 0$. For intermediate interaction strength, the P phase emerges with $I_z^{\parallel} \neq 0$, as shown in Fig. 4(a), and the mirror symmetry is spontaneously broken. The P phase may also support vortex currents, leading to a large rung current order $I_{0s}^{\perp}$. Different phases have different spin occupations; therefore, the spin-moment orders also exhibit sharp transitions at the phase boundary, as shown in Fig. 4(b).

Besides the currents and spin moments, the von Neumann entropy S_{vN} and the low-energy-level spacing Δ_i can also signal the transitions. When the entanglement entropy S_{vN}, an analytic function of correlations, is not analytic at some point (S_{vN} or its derivatives show discontinuity) [43], it must correspond to a quantum phase transition (as long as the definition of the entanglement entropy is analytic at that point). Although strict nonanalyticity is expected in the thermodynamic limit, we find that sharp features in the entropy emerge at the critical phase transition points with a finite-size system, as demonstrated in Fig. 4(c), confirming the positions of the phase transitions. The degeneracy of the ground state can be seen from low-energy-level spacing, which signals the
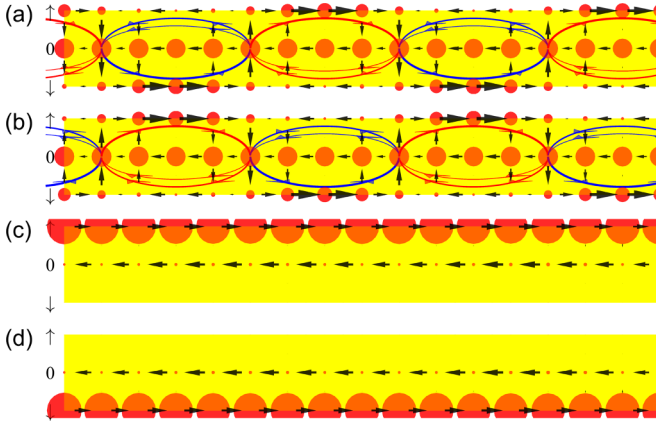
FIG. 5. (a)–(d) Schematics of the density distributions $n_{j,\sigma}$ and currents $J_{j,\sigma}^{\parallel}$ and $J_{j,0s}^{\perp}$ of the fourfold-degenerate ground state in the P phase, respectively. In all plots, we have $\Omega/t = 0.2$, $\phi/\pi = 1/4$, $U_0/t = 4.0$, $U_2 = -0.2U_0$, $\rho = 1.0$, and $L = 64$ (only the central 17 sites are shown in the plot).

spontaneous symmetry breaking across the phase transition. As demonstrated in Fig. 4(d), Δ_i vanish for $i < 4$ in the P phase due to ground-state degeneracy. The interaction can drive the system from the V phase (in the weak-interaction regime) to the M phase (in the strong-interaction regime), although the lowest single-particle band has two minima. Different from the noninteracting V phase, in which the ground state is an arbitrary linear combination of the two band minima, here, the interacting V phase is stabilized by ferromagnetic spin-spin interaction, leading to an equal superposition of the two band minima. On the one hand, the interference between two band minima would induce density modulation and increase density-density interaction energy. On the other hand, the superposition also generates spin orders which lower the ferromagnetic spin-spin interaction energy, and the system favors the V phase since the spin-spin interaction dominates over the density-density interaction. We note that, for the V phase in the weak-interaction region, the mean-field analysis predicts that the relative phase between atoms at two band minima can be either 0 or π [25] and the ground states should be twofold degenerate and are related to each other by shifting the vortex by half a period along the leg direction. However, such degeneracy is lifted by the finite-size and finite-n_{cutoff} effects. In the strong-interaction regime, the atom distribution in momentum space is broadened, and the two wave packets at the two band minima merge into one centered at $q = 0$; therefore, the system favors the M phase even when the lowest band has two minima. The current distributions of the interacting M and V phases are very similar to that for the noninteracting case shown in Figs. 3(a) and 3(b3).

Interestingly, a novel P phase emerges at intermediate interaction strength. The typical current and density distributions are shown in Fig. 5 for flux $\phi/\pi = 1/4$. In this P phase, the mirror symmetry with respect to the middle leg is spontaneously broken, and atoms start to occupy the dark middle band with $n_- \neq 0$. In addition to the mirror symmetry, the Z_2 exchange symmetry $|0\rangle \leftrightarrow |+\rangle$ is also broken, leading to a fourfold degeneracy of the ground states. The symmetry breaking can be seen from the spin moments in Fig. 4(b) with
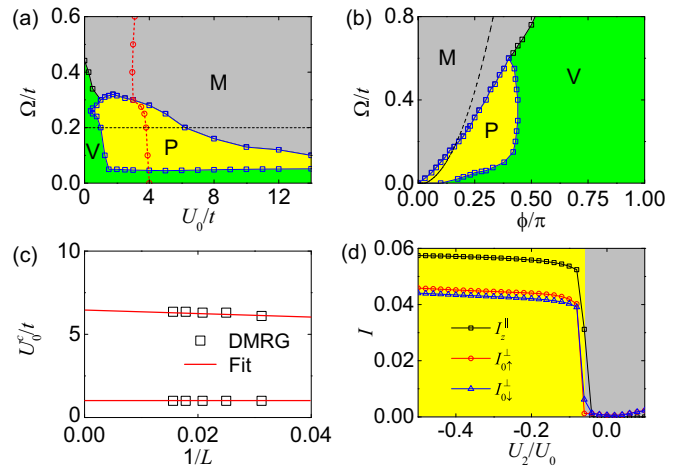

FIG. 6. The phase diagrams in the planes (a) Ω-U_0 with $\phi/\pi = 1/4$ and (b) Ω-ϕ with $U_0/t = 2$. The red dashed line in (a) is the phase transition point between the superfluid (left side) and Mott-insulator (right side) phases; order parameters along the black dashed horizontal line in (a) are shown in Fig. 4. The black dashed line in (b) is the single-particle phase boundary. (c) The finite-size scaling of the critical points U_0^c/t of the phase transitions, with $\Omega/t = 0.2$ and $\phi/\pi = 1/4$. In (a)–(c), $U_2 = -0.2U_0$. (d) The current order parameters $I_z^{\parallel}$ and $I_{0s}^{\perp}$ versus interaction strength U_2, with $\Omega/t = 0.2$, $\phi/\pi = 1/4$, $U_0/t = 2.0$, and $L = 64$. In all plots, we have $\rho = 1.0$.

$n_0 \neq n_+$ and also the density distributions in Fig. 5, which indicate that $n_{j\uparrow} \neq n_{j\downarrow}$. Notice that the M and V phases preserve the mirror symmetry and Z_2 exchange symmetry with $n_0 = n_+$ and $n_\uparrow = n_\downarrow$. The P phase can be a combined population of the middle band with either a left minimum [Figs. 5(a) and 5(b)] or a right minimum [Figs. 5(c) and 5(d)] of the lowest band, and for either combination, the polarization $S_{j,z} = n_{j,\uparrow} - n_{j,\downarrow}$ is nonvanishing and can be either positive or negative (related to the mirror symmetry), which is determined by the relative phase between atoms on the two bands. For the two ground states with a dominate population on the left minimum of the lowest band, vortex-antivortex pairs are formed along the leg direction, leading to modulations of spin densities and currents with period $2\pi/\phi$. We note that the order parameters of the P phase in Figs. 4(a)–4(c) are obtained from the vortex ground state. Moreover, due to the breaking mirror symmetry, the local spin-vector current $\sum_\sigma \sigma J_{j,\sigma}^{\parallel}$ and spin-tensor current $\sum_\sigma \sigma^2 J_{j,\sigma}^{\parallel}$ are both finite in the P phase. This dark middle band has a spin state orthogonal to the lowest band, so the superposition of the two bands will induce only spin orders without generating density modulation. Note that both the P and V phases have a lower spin-spin interaction energy and the P phase has a higher single-particle energy but a lower density-density interaction energy compared to the V phase; therefore, a transition from the V to P phase occurs as we increase the density-density interaction strength.

In Figs. 6(a) and 6(b), we map the phase diagrams in the Ω-U_0 plane with $\phi/\pi = 1/4$ and in the Ω-ϕ plane with $U_0/t = 2$, respectively. We see that the M phase area is enlarged by interactions. Figure 6(a) clearly shows that the V and P phases are replaced eventually by the M phase as the interaction strength increases. The system favors the P phase

for weak interleg coupling Ω and small flux ϕ, where the dark middle band can be occupied more easily since the energy gap with the lowest band is small. For very small Ω, the mixing between states $|0\rangle$ and $|+\rangle$ is also weak, so the density modulation and therefore the density-density interaction energy in the V phase are weak, and the system favors the V phase instead of the P phase, which has higher single-particle energy. Similarly, when the flux is large, density-density interaction energy for the V phase is small compared to the high single-particle energy in the P phase, and the system favors V over the P phase, as shown in Fig. 6(b). As Ω increases across some critical value, the density-density interaction energy for the V phase becomes stronger compared to the ferromagnetic spin-spin interaction energy; atoms will spontaneously populate around one of the two band minima with a single wave packet centered around $q \neq 0$, and the system enters the M phase. Further increasing Ω will drive the wave-packet center to $q = 0$. For a small flux, the system may directly enter the M phase with one wave packet centered at $q = 0$. In this paper, we do not distinguish the two different types of M phases (centered around $q = 0$ and $q \neq 0$) since they have similar current distributions.

To obtain the phase diagram, we employed the finite-size scaling, leading to the critical points of phase transitions in the thermodynamic limit, which are almost the same as those of finite-size systems, as shown in Fig. 6(c). The finite-size effects of the order parameters as well as the energy-level spacing and gap are discussed in Appendix B. As we discussed previously, the V and P phases result from the ferromagnetic spin-spin interaction. For antiferromagnetic spin-spin interactions $U_2/U_0 > 0$, one has only the M phase. To see this, we plot the current order parameters as a function of spin-dependent interaction strength U_2 in Fig. 6(d), showing that the P phase exists only in the ferromagnetic region. We want to emphasize that the Meissner currents induced by the gauge field persist even when the system enters the Mott-insulator region; the red dashed line in Fig. 6(a) shows the boundary between the superfluid and Mott-insulator phases, which is obtained by calculating the chemical potential gap [52–55].

IV. DISCUSSION AND CONCLUSION

Experimentally, the spin moments can be measured by population imaging after Stern-Gerlach separation [16,18]. The currents can be observed by site-resolved detection of the quench dynamics [14]. The current (motion of atoms) can also be proved by spin-selective time-of-flight imaging of the lattice momentum distribution [14,15]

$$n_\sigma(k) = \sum_{i,j} e^{ik(i-j)} \langle \hat{b}_{i\sigma}^\dagger \hat{b}_{j\sigma} \rangle. \tag{11}$$

The current is related to the lattice momentum unbalance, and we can define the chirality of the atomic motion as

$$\chi_\sigma = \frac{1}{L} \int_0^\pi h_\sigma(k) dk, \tag{12}$$

which shows behaviors similar to the current $J_\sigma^\parallel$ [15,21], where $h_\sigma(k) = n_\sigma(k) - n_\sigma(-k)$ is the asymmetry function. Moreover, the entanglement entropy can be measured using

quantum interference of many-body twins of ultracold atoms in optical lattices [42].

In summary, we studied the Meissner effects of interacting bosons in a one-dimensional optical lattice with spin-tensor–momentum coupling. Using the state-of-the-art density-matrix renormalization-group numerical method, we obtained a phase diagram with a rich variety of interesting phases, including the Meissner, vortex, and polarized phases. The current distributions show spin-tensor properties and interesting vortex structures that are unique for the spin-tensor–momentum coupled system with high spin, which may have possible applications in atomic spintronic devices. Our work revealed nontrivial phases and transport properties resulting from the interplay between spin tensors, lattice physics, and interactions and thus paves the way for exploring novel many-body phenomena of interacting particles in nonuniform gauge fields.

APPENDIX A: EFFECTS OF n_{cutoff}

As we discussed in the main text, the cutoff of the single-site atom number n_{cutoff} modifies the phase and phase boundary in the weak-interaction region. A larger n_{cutoff} leads to more accurate results, but the calculation becomes more computationally expensive. In Fig. 7, we show the order parameter n_- as a function of U_0 with different atom-number cutoffs. We see that the results are nearly the same in the region where $U_0/t > 1.5$ for $n_{\text{cutoff}} = 3, 4, 5$, while in the weak-interaction region where $U_0/t < 1$, the results for $n_{\text{cutoff}} = 3$ deviate significantly from that for $n_{\text{cutoff}} = 4, 5$. This can be easily understood by noticing that, for weaker interaction, the probability of high occupation is larger in the ground state. On the other hand, we find that the results for
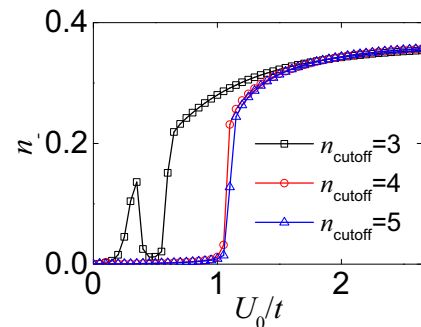

FIG. 7. Spin moment order n_- as a function of interaction strength U_0/t for several n_{cutoff}, with $\Omega/t = 0.2$, $\phi/\pi = 1/4$, $U_2 = -0.2U_0$, $\rho = 1.0$, and $L = 32$.
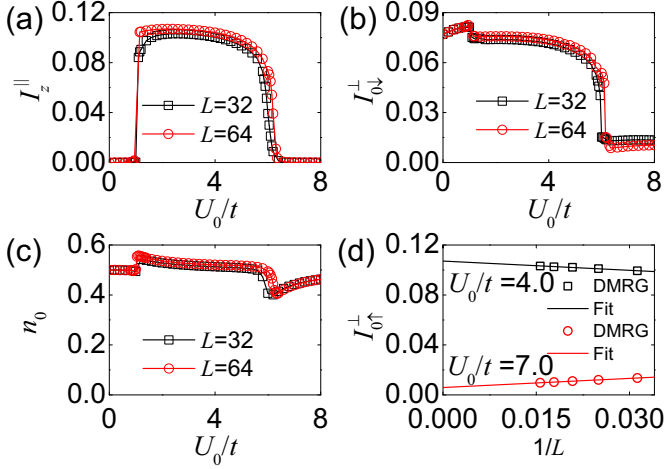
FIG. 8. (a) The current order parameter $I_z^{\parallel}$, (b) the current order parameter $I_{0\downarrow}^{\perp}$, and (c) the spin-moment order n_0 versus U_0 for $L = 32$ and 64. (d) The finite-size scaling of $I_{0\uparrow}^{\perp}$ for $U_0/t = 4.0$ and 7.0. In all plots, we have $\Omega/t = 0.2$, $\phi/\pi = 1/4$, $U_2 = -0.2U_0$, and $\rho = 1.0$.

FIG. 9. (a) Entropy S_{vN} versus U_0/t for $L = 32$ and 64. (b) Δ_i versus U_0/t for $L = 32$. The finite-size scaling of Δ_i for (c) the V phase with $U_0/t = 0.6$ and the M phase with 7.0 and (d) the P phase with $U_0/t = 3.0$ and 5.2. In all plots, we have $\Omega/t = 0.2$, $\phi/\pi = 1/4$, $U_2 = -0.2U_0$, and $\rho = 1.0$. The units of Δ_i are t.

$n_{\text{cutoff}} = 4$ and $n_{\text{cutoff}} = 5$ are nearly the same (both give a phase boundary around $U_0/t = 1$), indicating that $n_{\text{cutoff}} = 4$ is enough to determine the phase boundaries (note that most of the phase boundaries are located in the region where $U_0/t \geqslant 1$ in the phase diagram).

APPENDIX B: FINITE-SIZE EFFECTS

Now we briefly discuss the finite-size effects on the order parameters. As the system size increases, the order parameters may be slightly modified (especially near the critical phase boundaries), and thus, the phase boundaries (determined by examining the spontaneous symmetry breaking) may shift slightly as we increase the size. The phase boundaries at the thermodynamic limit are obtained by finite-size scaling [see Fig. 6(c)]. In Figs. 8(a)–8(c), we plot the order parameters as a function of U_0 for system sizes $L = 32$ and $L = 64$; away from the phase boundaries, we see that the order parameters are almost the same for the different sizes. In Fig. 8(d), we plot the typical finite-size scaling of the order parameters and find that the thermodynamic value is very close to the finite-size value with $L = 64$. We note that the rung current in the M phase [see the red line in Fig. 8(d)] decreases as the system size increases; that is, because the leg currents must form a closed loop at the boundary through the rungs, such a boundary-rung current leads to an average rung current scaling as $1/L$. Numerically, we find that the average rung current $I_{0s}^{\perp}$ does not vanish completely in the M phase (although it is extremely small). For such an interaction-driven M phase, although atoms occupy a single broadened wave packet in momentum space, the double-well structure of the
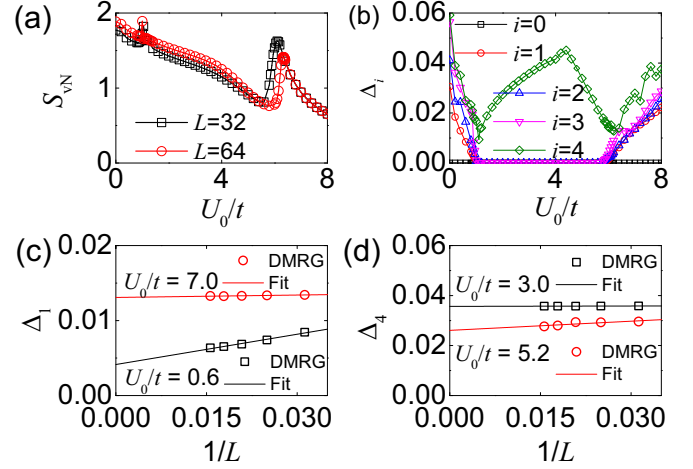
lowest band may result in residual interference that leads to the tiny rung current.

As we discussed in the main text, the von Neumann entropy S_{vN} and the low-energy-level spacing Δ_i can also signal phase transitions. For different system sizes, the entropy S_{vN} exhibits similar curves, with peak positions always matching the phase boundaries given by the order parameters (currents and spin moments), as shown in Fig. 9(a) for $L = 32$ and 64. For the low-energy-level spacing, we showed the results for $L = 64$ in the main text; while the results for $L = 32$ are similar [see Fig. 9(b)], the fourfold degeneracy is clearly seen in the P phase. To see how the energy gap scales with the system size, we plot the finite-size scaling results in Figs. 9(c) and 9(d); note that the energy gap corresponds to Δ_1 (Δ_4) for the V and M phases (P phase). The small gaps in the P and M phases change slightly with system size and remain finite (of the order of $\sim 10^{-2}t$) in the thermodynamic limit, vanishing at their phase boundary. However, for the V phase, the gap decreases significantly with increasing system size, reaching a small value (of the order of $10^{-3}t$) in the thermodynamic limit. We also note that, in the V phase, higher excited-state energy gaps Δ_i ($i > 1$) also decrease with increasing system size; the low-energy levels are nearly equally spaced in the thermodynamic limit. Since the V phase appears in the weak-interaction region where the effects of cutoff n_{cutoff} are more significant, we believe that the tiny gap in the V phase may be induced by the cutoff, and the V phase is probably a gapless phase.

[1] M. Hasan and C. Kane, Colloquium: Topological insulators, Rev. Mod. Phys. **82**, 3045 (2010).

[2] X.-L. Qi and S.-C. Zhang, Topological insulators and superconductors, Rev. Mod. Phys. **83**, 1057 (2011).

[3] W. Braunisch, N. Knauf, V. Kataev, S. Neuhausen, A. Grütz, A. Kock, B. Roden, D. Khomskii, and D. Wohlleben, Paramagnetic Meissner Effect in Bi High-Temperature Superconductors, Phys. Rev. Lett. **68**, 1908 (1992).

[4] A. K. Geim, S. V. Dubonos, J. G. S. Lok, M. Henini, and J. C. Maan, Paramagnetic Meissner effect in small superconductors, Nature (London) **396**, 144 (1998).

[5] Y.-J. Lin, K. Jiménez-García, and I. B. Spielman, Spin-orbit coupled Bose-Einstein condensates, Nature (London) **471**, 83 (2011).

[6] P. Wang, Z. Q. Yu, Z. Fu, J. Miao, L. Huang, S. Chai, H. Zhai, and J. Zhang, Spin-Orbit Coupled Degenerate Fermi Gases, Phys. Rev. Lett. **109**, 095301 (2012).

[7] L. Cheuk, A. Sommer, Z. Hadzibabic, T. Yefsah, W. Bakr, and M. Zwierlein, Spin-Injection Spectroscopy of a Spin-Orbit Coupled Fermi Gas, Phys. Rev. Lett. **109**, 095302 (2012).

[8] C. Hamner, Y. Zhang, M. A. Khamehchi, M. J. Davis, and P. Engels, Spin-Orbit-Coupled Bose-Einstein Condensates in a One-Dimensional Optical Lattice, Phys. Rev. Lett. **114**, 070401 (2015).

[9] L. Huang, Z. Meng, P. Wang, P. Peng, S.-L. Zhang, L. Chen, D. Li, Q. Zhou, and J. Zhang, Experimental realization of two-dimensional synthetic spin-orbit coupling in ultracold Fermi gases, Nat. Phys. **12**, 540 (2016).

[10] Z. Wu, L. Zhang, W. Sun, X.-T. Xu, B.-Z. Wang, S.-C. Ji, Y. Deng, S. Chen, X.-J. Liu, and J.-W. Pan, Realization of two dimensional spin-orbit coupling for Bose-Einstein condensates, Science **354**, 83 (2016).

[11] J.-R. Li, J. Lee, W. Huang, S. Burchesky, B. Shteynas, F. C. Top, A. O. Jamison, and W. Ketterle, A stripe phase with supersolid properties in spin-orbit-coupled Bose-Einstein condensates, Nature (London) **543**, 91 (2017).

[12] S. Kolkowitz, S. L. Bromley, T. Bothwell, M. L. Wall, G. E. Marti, A. P. Koller, X. Zhang, A. M. Rey, and J. Ye, Spin-orbit coupled fermions in an optical lattice clock, Nature (London) **542**, 66 (2017).

[13] A. Petrescu and K. L. Hur, Bosonic Mott Insulator with Meissner Currents, Phys. Rev. Lett. **111**, 150601 (2013).

[14] M. Atala, M. Aidelsburger, M. Lohse, J. T. Barreiro, B. Paredes, and I. Bloch, Observation of chiral currents with ultracold atoms in bosonic ladders, Nat. Phys. **10**, 588 (2014).

[15] M. Mancini, G. Pagano, G. Cappellini, L. Livi, M. Rider, J. Catani, C. Sias, P. Zoller, M. Inguscio, M. Dalmonte, and L. Fallani, Observation of chiral edge states with neutral fermions in synthetic Hall ribbons, Science **349**, 1510 (2015).

[16] B. K. Stuhl, H.-I. Lu, L. M. Aycock, D. Genkina, and I. B. Spielman, Visualizing edge states with an atomic Bose gas in the quantum Hall regime, Science **349**, 1514 (2015).

[17] O. Boada, A. Celi, J. I. Latorre, and M. Lewenstein, Quantum Simulation of an Extra Dimension, Phys. Rev. Lett. **108**, 133001 (2012).

[18] A. Celi, P. Massignan, J. Ruseckas, N. Goldman, I. B. Spielman, G. Juzeliūnas, and M. Lewenstein, Synthetic Gauge Fields in Synthetic Dimensions, Phys. Rev. Lett. **112**, 043001 (2014).

[19] H. M. Price, O. Zilberberg, T. Ozawa, I. Carusotto, and N. Goldman, Four-Dimensional Quantum Hall Effect with Ultra-cold Atoms, Phys. Rev. Lett. **115**, 195303 (2015).

[20] H. Zhai, Degenerate quantum gases with spin-orbit coupling: A review, Rep. Prog. Phys. **78**, 026001 (2015).

[21] L. F. Livi, G. Cappellini, M. Diem, L. Franchi, C. Clivati, M. Frittelli, F. Levi, D. Calonico, J. Catani, M. Inguscio, and L. Fallani, Synthetic Dimensions and Spin-Orbit Coupling with an Optical Clock Transition, Phys. Rev. Lett. **117**, 220401 (2016).

[22] H. M. Bharath, Non-Abelian geometric phases carried by the spin fluctuation tensor, J. Math. Phys. **59**, 062105 (2018).

[23] H. M. Bharath, M. Boguslawski, M. Barrios, L. Xin, and M. S. Chapman, Exploring Non-Abelian Geometric Phases in Spin-1 Ultracold Atoms, Phys. Rev. Lett. **123**, 173202 (2019).

[24] D. Li, L. Huang, P. Peng, G. Bian, P. Wang, Z. Meng, L. Chen, and J. Zhang, Experimental realization of a spin-tensor momentum coupling in ultracold Fermi gases, Phys. Rev. A **102**, 013309 (2020).

[25] X.-W. Luo, K. Sun, and C. Zhang, Spin-Tensor–Momentum-Coupled Bose-Einstein Condensates, Phys. Rev. Lett. **119**, 193001 (2017).

[26] X.-Y. Mai, Y.-Q. Zhu, Z. Li, D.-W. Zhang, and S.-L. Zhu, Topological metal bands with double-triple-point fermions in optical lattices, Phys. Rev. A **98**, 053619 (2018).

[27] H. Hu, J. Hou, F. Zhang, and C. Zhang, Topological Triply Degenerate Points Induced by Spin-Tensor-Momentum Couplings, Phys. Rev. Lett. **120**, 240401 (2018).

[28] Z. Lei, Y. Deng, and C. Lee, Unpaired topological triply degenerate point for spin-tensor-momentum-coupled ultracold atoms, Phys. Rev. Res. **4**, 033008 (2022).

[29] M. Zhang, X. Yuan, Y. Li, X.-W. Luo, C. Liu, M. Zhu, X. Qin, C. Zhang, Y. Lin, and J. Du, Observation of Spin-Tensor Induced Topological Phase Transitions of Triply Degenerate Points with a Trapped Ion, Phys. Rev. Lett. **129**, 250501 (2022).

[30] X. Zhou, X.-W. Luo, G. Chen, S. Jia, and C. Zhang, Quantum spiral spin-tensor magnetism, Phys. Rev. B **101**, 140412(R) (2020).

[31] S. R. White, Density Matrix Formulation for Quantum Renormalization Groups, Phys. Rev. Lett. **69**, 2863 (1992).

[32] U. Schollwöck, The density-matrix renormalization group, Rev. Mod. Phys. **77**, 259 (2005).

[33] T. L. Ho, Spinor Bose Condensates in Optical Traps, Phys. Rev. Lett. **81**, 742 (1998).

[34] T. Ohmi and K. Machida, Bose-Einstein condensation with internal degrees of freedom in alkali atom gases, J. Phys. Soc. Jpn. **67**, 1822 (1998).

[35] S. Barbarino, L. Taddia, D. Rossini, L. Mazza, and R. Fazio, Magnetic crystals and helical liquids in alkaline-earth fermionic gases, Nat. Commun. **6**, 8134 (2015).

[36] X. Zhou, J.-S. Pan, W. Yi, G. Chen, and S. Jia, Interaction-induced exotic vortex states in an optical lattice clock with spin-orbit coupling, Phys. Rev. A **96**, 023627 (2017).

[37] S. T. Flammia, A. Hamma, T. L. Hughes, and X.-G. Wen, Topological Entanglement Rényi Entropy and Reduced Density Matrix Structure, Phys. Rev. Lett. **103**, 261601 (2009).

[38] M. B. Hastings, I. González, A. B. Kallin, and R. G. Melko, Measuring Rényi Entanglement Entropy in Quantum Monte Carlo Simulations, Phys. Rev. Lett. **104**, 157201 (2010).

[39] A. J. Daley, H. Pichler, J. Schachenmayer, and P. Zoller, Measuring Entanglement Growth in Quench Dynamics of Bosons in an Optical Lattice, Phys. Rev. Lett. **109**, 020505 (2012).

[40] D. A. Abanin and E. Demler, Measuring Entanglement Entropy of a Generic Many-Body System with a Quantum Switch, Phys. Rev. Lett. **109**, 020504 (2012).

[41] H.-C. Jiang, Z.-H. Wang, and L. Balents, Identifying topological order by entanglement entropy, Nat. Phys. **8**, 902 (2012).

[42] R. Islam, R. Ma, P. M. Preiss, M. E. Tai, A. Lukin, M. Rispoli, and M, Greiner, Measuring entanglement entropy in a quantum many-body system, Nature (London) **528**, 77 (2015).

[43] L. Amico, R. Fazio, A. Osterloh, and V. Vedral, Entanglement in many-body systems, Rev. Mod. Phys. **80**, 517 (2008).

[44] C. Chin, R. Grimm, P. Julienne, and E. Tiesinga, Feshbach resonances in ultracold gases, Rev. Mod. Phys. **82**, 1225 (2010).

[45] S. Raghu, X.-L. Qi, C. Honerkamp, and S.-C. Zhang, Topological Mott Insulators, Phys. Rev. Lett. **100**, 156401 (2008).

[46] I. Bloch, J. Dalibard, and W. Zwerger, Many-body physics with ultracold gases, Rev. Mod. Phys. **80**, 885 (2008).

[47] E. J. Mueller, Review of pseudogaps in strongly interacting Fermi gases, Rep. Prog. Phys. **80**, 104401 (2017).

[48] S. Rachel, Interacting topological insulators: A review, Rep. Prog. Phys. **81**, 116501 (2018).

[49] J. Jünemann, A. Piga, S.-J. Ran, M. Lewenstein, M. Rizzi, and A. Bermudez, Exploring Interacting Topological Insulators with Ultracold Atoms: The Synthetic Creutz-Hubbard Model, Phys. Rev. X **7**, 031057 (2017).

[50] X. Zhou, J.-S. Pan, Z.-X. Liu, W. Zhang, W. Yi, G. Chen, and S. Jia, Symmetry-Protected Topological States for Interacting Fermions in Alkaline-Earth-Like Atoms, Phys. Rev. Lett. **119**, 185701 (2017).

[51] S. de Léséleuc, V. Lienhard, P. Scholl, D. Barredo, S. Weber, N. Lang, H. P. Büchler, T. Lahaye, and A. Browaeys, Observation of a symmetry-protected topological phase of interacting bosons with Rydberg atoms, Science **365**, 775 (2019).

[52] J. K. Freericks and H. Monien, Strong-coupling expansions for the pure and disordered Bose-Hubbard model, Phys. Rev. B **53**, 2691 (1996).

[53] T. D. Kühner and H. Monien, Phases of the one-dimensional Bose-Hubbard model, Phys. Rev. B **58**, R14741(R) (1998).

[54] T. D. Kühner, S. R. White, and H. Monien, One-dimensional Bose-Hubbard model with nearest-neighbor interaction, Phys. Rev. B **61**, 12474 (2000).

[55] M. Rizzi, D. Rossini, G. De Chiara, S. Montangero, and R. Fazio, Phase Diagram of Spin-1 Bosons on One-Dimensional Lattices, Phys. Rev. Lett. **95**, 240404 (2005).